Journal of Mathematical Imaging and Vision manuscript No.
(will be inserted by the editor)

Decoupled Algorithm for MRI Reconstruction using Nonlocal Block Matching Model: BM3D-MRI

Ender M. Eksioglu

Received: date / Accepted: date

Abstract The Block Matching 3D (BM3D) is an efficient image model, which has found few applications other than its niche area of denoising. We will develop a Magnetic Resonance Imaging (MRI) reconstruction algorithm, which uses decoupled iterations alternating over a denoising step realized by the BM3D algorithm and a reconstruction step through an optimization formulation. The decoupling of the two steps allows the adoption of a strategy with a varying regularization parameter, which contributes to the reconstruction performance. This new iterative algorithm efficiently harnesses the power of the nonlocal, image-dependent BM3D model. The MRI reconstruction performance of the proposed algorithm is superior to state-of-the-art algorithms from the literature. A convergence analysis of the algorithm is also presented.

Keywords Image reconstruction · magnetic resonance · block matching · BM3D · compressed sensing · sparsity

1 Introduction

Ill-posed inverse problems in image restoration and reconstruction have been a fertile ground for the application of various regularization methods. These image processing applications include but are not limited to denoising, deblurring, demosaicking, inverse halftoning, single or multi-image superresolution, inpainting, and various image reconstruction problems such as magnetic resonance imaging (MRI) and computerized tomography (CT) [16]. The observation or data acquisition forward model for all of these image restoration modalities can eventually be approximated as a discretized linear system [16].

$$\mathbf{y} = \mathbf{A}\mathbf{x}^\star + \boldsymbol{\eta} \tag{1}$$

$\mathbf{x}^\star \in \mathbb{C}^N$ denotes the original or desired image to be restored, in a vectorized form. The observed data is given as the vector $\mathbf{y} \in \mathbb{C}^\kappa$. The linear operator $\mathbf{A} : \mathbb{C}^N \to \mathbb{C}^\kappa$ formulates the observation forward model for the particular image processing paradigm. The various image restoration and reconstruction paradigms as listed above result in diverse $\mathbf{A}$ matrices for the forward observation model. Possible $\mathbf{A}$ matrices include an identity operator for denoising, convolution operators for deblurring, filtered subsampling operators for superresolution or the Fourier k-domain subsampling operator for MRI reconstruction. The backward program of reconstructing an estimate of $\mathbf{x}^\star$ is usually an ill-posed problem. The ill-posedness of the backward estimation might be because the problem is underdetermined with $N > \kappa$. On the other hand, the inverse problem might also be nonstable due to a numerically ill-conditioned operator $\mathbf{A}$ and the presence of noise. Whatever the reason for the ill-posedness of the inverse problem, regularization of the problem is a viable approach to reach a good estimate of $\mathbf{x}^\star$. The variational formulation for regularization of the inverse problem, assumes the addition of a penalty function to the cost function getting minimized [16].

$$\min_{\mathbf{x}} \|\mathbf{A}\mathbf{x} - \mathbf{y}\|_2^2 + \lambda\rho(\mathbf{x}). \tag{2}$$

Here, we would like to call $\|\mathbf{A}\mathbf{x} - \mathbf{y}\|_2^2$ as the observation fidelity term, as it ensures the concurrence of the restored image $\mathbf{x}$ with the observation $\mathbf{y}$. The ℓ_2 norm

Ender M. Eksioglu
Electronics and Communications Engineering Department, Istanbul Technical University, Istanbul, Turkey
Tel./Fax: +90-212-285 3623
E-mail: eksioglue@itu.edu.tr

presumes normal distribution for the additive noise $\boldsymbol{\eta}$. The penalty function $\rho(\cdot)$ enforces some a priori knowledge about the latent image $\mathbf{x}^\star$ into action. Usually the regularization function might depend on transform domain coefficients of the image, where the transform is a nonadaptive, linear operator acting on the image. It is often the case that the dependency on the transform coefficients is via a norm function. Hence, one viable option for the regularization penalty is as follows.

$$\rho(\mathbf{x}) = \|\mathbf{W}\mathbf{x}\|_p^p. \tag{3}$$

Here, $\mathbf{W}$ is a linear transform operator. For $p = 2$ the resulting regularization is the well-studied Tikhonov regularization. Other recently popular choices to use in (3) are the sparsity inducing ℓ_0 and ℓ_1 norms. The penalty function, given in terms of the nonadaptive transform domain coefficients, should highlight some sort of structure known to be inherent to the latent image. One prevalent alternative for the nonadaptive transform has been the wavelet transform, which preserves scale-invariant structures in the image [3]. On the other hand, a piecewise-constant assumption for the latent image leads to the use of derivative functions for the nonadaptive transform. A two-dimensional (2D) first-order derivative, discretized as a first-order difference operation, leads to the Total Variation (TV) minimization methods [4].

For example, the sparsity regularized MRI reconstruction problem has been described as given below [20],

$$\min_{\mathbf{x}} \tfrac{1}{2}\|\boldsymbol{\mathcal{F}}_u\mathbf{x} - \mathbf{y}\|_2^2 + \beta_1\|\boldsymbol{\Theta}\mathbf{x}\|_1 + \beta_2\|\mathbf{x}\|_{\mathrm{TV}} \tag{4}$$

where the operator $\boldsymbol{\mathcal{F}}_u : \mathbb{C}^N \to \mathbb{C}^\kappa$, with $\kappa < N$, denotes the subsampled Fourier transform. In this cost function, which is regularized by a composite penalty function $\rho(\cdot)$, $\boldsymbol{\Theta}$ is an orthogonal wavelet transform, $\|\cdot\|_{\mathrm{TV}}$ denotes the TV measure, and β_1 and β_2 are the regularization parameters. This compressed sensing (CS) or sparse MRI cost function has been studied in various papers [17,20–22,24,31], leading to an assortment of solvers. Sparse MRI provides an effective regularization framework for solving the MRI reconstruction problem. A distinct line of work has considered the parallel MRI reconstruction problem resulting in multicoil parallel MRI algorithms such as SENSE [23] and GRAPPA [15].

The nonadaptive models using fixed regularizers such as the wavelet transform or the TV seminorm have been quite popular. However, there are more recent, data-dependent and nonlocal image models which offer better performance. There have been MRI reconstruction algorithms based on the nonlocal processing paradigm. The Low dimensional-structure Self-learning and Thresholding (LOST) algorithm as introduced in [1] and the more recent Patch-based Nonlocal Operator (PANO) algorithm of [25] are examples for such nonlocal MRI algorithms. Another recent popular line of algorithms for solving reconstruction problems have used denoising as an explicit substep. One of the earliest examples for this approach has been the decoupled deblurring and denoising algorithm of [30]. Another more recent denoising based algorithm is the plug-and-play prior framework which has been applied to bright field electron tomography [28]. A different algorithm which uses denoising as a substep is the Approximate Message Passing (AMP) with image denoising algorithm which has been applied to compressive imaging [29].

The Block Matching 3D (BM3D) image model facilitates nonlocal structures in the image by using groupings of image patches. The BM3D model has first been introduced in the image denoising setting with great success [7]. Despite its state-of-the-art performance in image denoising, further applications of the BM3D model have been limited. To the best of our knowledge, applications for the BM3D model other than denoising include deblurring [8,10,11,18], inpainting [19], superresolution [9], tomographic reconstruction [12] and compression [6]. In this paper we intend to harness the power of the BM3D image model as a regularizer for the MRI reconstruction problem. We will utilize the BM3D model inside a novel algorithm which decouples the observation fidelity and model fidelity steps, as we will call them. The decoupling will be based on the decoupled deblurring and denoising algorithm of [30].

The outline of the rest of the paper is as follows. In Section 2, we will give a summary of the decoupled algorithm and the BM3D image model, which we will adopt. Section 3 develops the novel MRI reconstruction algorithm we propose. We discuss the convergence and implementation details of the proposed algorithm in Section 4. The simulations in Section 5 compare the MRI reconstruction performance of the proposed algorithm against state-of-the-art methods from the literature. We conclude the paper with an overview of the proposed method and possible research directions.

2 The decoupled algorithm and the image model

2.1 Decoupled algorithm for image restoration and reconstruction

The regularized minimization problem (2) has been the target of various optimization approaches. In general these optimization procedures bargain a tradeoff between the observation fidelity term and the prior structure enforcement term. An efficient algorithm for solving regularized image restoration problems has been presented in [30]. The strength of this algorithm lies in the fact it explicitly decouples the two steps for enforcing the two individual components of the regularized cost function (2). The individual steps which get iterated in this algorithm can be given as follows [30].

$$\hat{\mathbf{x}}_i = \underset{\mathbf{x}}{\operatorname{argmin}} \ \|\mathbf{A}\mathbf{x} - \mathbf{y}\|_2^2 + \alpha\|\mathbf{x} - \mathbf{x}_{i-1}\|_2^2. \tag{5a}$$

$$\mathbf{x}_i = \underset{\mathbf{x}}{\operatorname{argmin}} \ \|\mathbf{x} - \hat{\mathbf{x}}_i\|_2^2 + \lambda\rho(\mathbf{x}). \tag{5b}$$

The first step (5a) updates the current estimate $\mathbf{x}_{i-1}$ as to better agree with the observation vector $\mathbf{y}$, where the regularization parameter α determines the degree of this agreement. The second step realizes a further update to better conform with the prior image model or structure as enforced by the penalty function $\rho(\mathbf{x})$. In [30], the forward matrix $\mathbf{A}$ has been assumed to be a blurring matrix, hence the algorithm has been used for deblurring. In this context, the two decoupled steps (5a) and (5b) have been called as the deblurring and denoising steps, respectively [30]. However, this two-step algorithm can in general be used for other image restoration and reconstruction problems. For a general forward model matrix $\mathbf{A}$, we would like to call the two steps as the observation fidelity and the model fidelity steps, respectively. In [30], the wavelet domain sparsity and the TV seminorm have been utilized as the prior structure enforcement terms in $\rho(\mathbf{x})$. We would like to employ other, more efficient image models. The BM3D as described in the next section provides such a more advanced image model.

2.2 Using BM3D as the image model

The BM3D approach provides an advanced image model which has been initially used for image denoising [7]. The BM3D image model is based on a nonlocal grouping of image patches (or blocks), and a subsequent 3D transformation of the resulting patch groups. In [7], where the BM3D model was first presented, the developed image denoising algorithm also included an additional collaborative Wiener filtering step. A more streamlined version of BM3D model which comprised only the main 3D transform shrinkage was presented in [11]. The framework as introduced in [11] is important, because the complicated BM3D model analysis operation gets summarized as a simple matrix multiplication with a proper non-tight frame. We want to repeat a brief summary of this analysis. For further details, one can consult [11]. The analysis equation for the BM3D image model in the case of a vectorized image is formulated as given below [11].

$$\boldsymbol{\omega} = \boldsymbol{\Phi}\mathbf{x} \tag{6}$$

Here, $\boldsymbol{\omega} \in \mathbb{C}^M$ is the joint 3D groupwise spectrum, which stores the 3D transform coefficients for patch groups extracted from the image. The patches (or blocks) extracted from the image are grouped together using a similarity criterion. The frame $\boldsymbol{\Phi} \in \mathbb{C}^{M \times N}$ with $M \gg N$ implements a highly overcomplete transform into the groupwise spectrum space. The backward transform from the groupwise spectrum space into the image space can be realized by a second frame, which basically inverts all the operations implemented by the analysis frame $\boldsymbol{\Phi}$ [11].

$$\mathbf{x} = \boldsymbol{\Psi}\boldsymbol{\omega} \tag{7}$$

$\boldsymbol{\Psi} \in \mathbb{C}^{N \times M}$ is the synthesis frame for the BM3D model. $\boldsymbol{\Phi}$ and $\boldsymbol{\Psi}$ are dual frames with $\boldsymbol{\Psi}\boldsymbol{\Phi} = \mathcal{I}_{N \times N}$ [11]. Both the analysis frame $\boldsymbol{\Phi}$ and the synthesis frame $\boldsymbol{\Psi}$ employ in their definitions the particular 3D transform applied on the patch groups. This 3D transform is chosen such that it is separable into a pair of 2D-intrablock and 1D-interblock subtransforms. These separate transforms efficiently exploit the data structure of the 3D patch cubes, and they also greatly reduce the computational complexity when compared with a nonseparable transform. These two subtransforms are nonadaptive, and they can be chosen freely from available transforms such as DCT, DFT or wavelet transforms among others. However, the definitions for these frames also depend on the distinct grouping structure of the extracted patches, which is unique for the particular image to be processed. Hence, the frames $\boldsymbol{\Phi}$ and $\boldsymbol{\Psi}$ are adaptive and image-dependent. This dependence of the analysis and synthesis frames on the processed image $\mathbf{x}$, is one of the reasons for the strength of the BM3D model.

3 BM3D-MRI Formulation

The frame representation of the BM3D image model has been applied to image deblurring in [11]. Here, we want to bring together the decoupled algorithm (5) of [30] and the BM3D image model. We will apply this novel approach to the MRI reconstruction problem. We specify the main iteration of our novel decoupled MRI reconstruction algorithm as follows.

$$\hat{\mathbf{x}}_i = \underset{\mathbf{x}}{\operatorname{argmin}} \ \|\boldsymbol{\mathcal{F}}_u\mathbf{x} - \mathbf{y}\|_2^2 + \alpha\|\mathbf{x} - \mathbf{x}_{i-1}\|_2^2. \tag{8a}$$

$$\mathbf{x}_i = \underset{\mathbf{x}}{\operatorname{argmin}} \ \|\mathbf{x} - \hat{\mathbf{x}}_i\|_2^2 + \lambda\|\boldsymbol{\Phi}_i\mathbf{x}\|_p \ . \tag{8b}$$

The BM3D analysis frame $\mathbf{\Phi}_i$ is adapted to the intermediary image $\hat{\mathbf{x}}_i$, at each iteration. One can use a constant frame $\mathbf{\Phi}$ created using the initial image estimate $\mathbf{x}_0$. This would result in a reduction both in complexity and reconstruction performance of the algorithm.

Now we will try to outline the solutions to the individual steps (8a) and (8b). The observation fidelity update (8a) has an exact least-squares solution. Solutions to similar problems have been discussed in the literature both in the MRI [26] and deblurring [11, 30] settings. The least-squares solution for (8a) will be given as the solution of the following equation.

$$(\boldsymbol{\mathcal{F}}_u^H\boldsymbol{\mathcal{F}}_u + \alpha\mathcal{I})\hat{\mathbf{x}}_i = \boldsymbol{\mathcal{F}}_u^H\mathbf{y} + \alpha\mathbf{x}_{i-1}. \tag{9}$$

Here, $\boldsymbol{\mathcal{F}}_u^H$ is the adjoint operator for the MRI observation matrix $\boldsymbol{\mathcal{F}}_u$. The vector $\boldsymbol{\mathcal{F}}_u^H\mathbf{y}$ is simply the zero-filling based reconstructed image for the given observed Fourier data $\mathbf{y}$. The partial Fourier matrix $\boldsymbol{\mathcal{F}}_u$ is diagonalized by the full Fourier matrix, such that $\boldsymbol{\mathcal{F}}\boldsymbol{\mathcal{F}}_u^H\boldsymbol{\mathcal{F}}_u\boldsymbol{\mathcal{F}}^H = \mathbf{\Lambda}$ is a diagonal matrix with ones and zeros on the diagonal. Here, $\boldsymbol{\mathcal{F}}$ is the full-sized, unitary Fourier matrix. $\mathbf{\Lambda}$ is only nonzero at the diagonal elements $k \in \mathbf{\Omega}$, where $\mathbf{\Omega}$ denotes the set of indices for Fourier data included in $\mathbf{y}$ [26]. If we use $\boldsymbol{\mathcal{F}}^H\boldsymbol{\mathcal{F}} = \boldsymbol{\mathcal{F}}\boldsymbol{\mathcal{F}}^H = \mathcal{I}$ and take the Fourier transform of both sides of (9), we end up with the following result:

$$\boldsymbol{\mathcal{F}}(\boldsymbol{\mathcal{F}}_u^H\boldsymbol{\mathcal{F}}_u + \alpha\mathcal{I})(\boldsymbol{\mathcal{F}}^H\boldsymbol{\mathcal{F}})\hat{\mathbf{x}}_i = \boldsymbol{\mathcal{F}}(\boldsymbol{\mathcal{F}}_u^H\mathbf{y} + \alpha\mathbf{x}_{i-1}). \tag{10}$$

$$\Rightarrow\ (\mathbf{\Lambda} + \alpha\mathcal{I})\boldsymbol{\mathcal{F}}\hat{\mathbf{x}}_i = \boldsymbol{\mathcal{F}}\boldsymbol{\mathcal{F}}_u^H\mathbf{y} + \alpha\boldsymbol{\mathcal{F}}\mathbf{x}_{i-1}. \tag{11}$$

We should note that the zero-filled Fourier domain vector $\boldsymbol{\mathcal{F}}\boldsymbol{\mathcal{F}}_u^H\mathbf{y}$ is zero for $k \notin \mathbf{\Omega}$. The simplified solution for (8a) is finalized as follows.

$$\boldsymbol{\mathcal{F}}\hat{\mathbf{x}}_i = \begin{cases} \boldsymbol{\mathcal{F}}\mathbf{x}_{i-1} & \text{, if } k \notin \mathbf{\Omega} \\ \dfrac{\boldsymbol{\mathcal{F}}\boldsymbol{\mathcal{F}}_u^H\mathbf{y} + \alpha\boldsymbol{\mathcal{F}}\mathbf{x}_{i-1}}{1+\alpha} & \text{, if } k \in \mathbf{\Omega} \end{cases} \tag{12}$$

This final equation, which is formalized in the k-space, is similar to the image update equation in [26]. The limit $\alpha \to 0$ corresponds to the noiseless observation case, with $\mathbf{y} = \boldsymbol{\mathcal{F}}_u\mathbf{x}^\star$. In this case, the Fourier coefficients of $\hat{\mathbf{x}}_i$ for $k \in \mathbf{\Omega}$ are simply restored to their original, observed values in $\mathbf{y}$. All the regularization parameters in equations (2), (4), (5) and (8) are positive valued in general. Of particular interest is (8a) with the α parameter. We calculate the solution for (8a) by using (12). If we consider (12) as the utilized solution for (8a), $\alpha = 0$ becomes a legitimate regularization parameter leading to a unique solution.

The model fidelity equation (8b) can be considered as a denoising problem with an analysis prior defined over the analysis frame $\mathbf{\Phi}_i$. There are various iterative algorithms for solving these type of problems, such as operator splitting methods [5] , split Bregman iterations [14] or the iterative frame shrinkage (IFS) algorithm [27]. If we consider only the very first iteration of the IFS algorithm [27] for solving this problem, this initial iteration will be calculated as follows:

$$\mathbf{x}_i = \mathbf{\Psi}_i\lfloor\mathbf{\Phi}_i\hat{\mathbf{x}}_i\rfloor_\lambda \tag{13}$$

In (13), the operator $\lfloor\cdot\rfloor_\lambda$ denotes the hard or soft thresholding operations for $p = 0$ and $p = 1$, respectively. This operator is calculated as follows [11].

$$\lfloor\boldsymbol{\omega}\rfloor_\lambda = \begin{cases} \boldsymbol{\omega} \circ (\boldsymbol{\omega} \geqq \sqrt{\lambda}\,), & p = 0 \\ \mathrm{sign}(\boldsymbol{\omega}) \circ \max(\boldsymbol{\omega} - \frac{\lambda}{2}, 0), & p = 1 \end{cases} \tag{14}$$

Here, "$\circ$" denotes an elementwise vector multiplication. We should note that equation (13) is simply the BM3D denoising algorithm formulated using the frame notation [11]. In our algorithm, we plan to use the frame shrinkage step (13) as an approximate solution for (8b). Hence, the model fidelity update of our algorithm will be realized by a BM3D based denoising of the input image.

Our proposed MRI reconstruction algorithm uses (8) and the corresponding solutions as its main iteration. This algorithm utilizes the nonlocal, patchwise block matching image model. We call this novel approach as the BM3D-MRI algorithm. A synopsis of the proposed BM3D-MRI algorithm is given in Alg.1. We should note that here we adopted a varying regularization parameter λ_j for model fidelity. This allows for a reconstruction method similar to the deterministic annealing based approaches [19], where the changing parameter allows for adaptivity to gradually uncover the underlying image structure. In Alg.1, the $\mathcal{J}$ parameter denotes the number of outer iterations where the λ parameter is varied as λ_j. The λ_j parameter decreases uniformly on a logarithmic scale starting from $\lambda_1 = \lambda_{\max}$ and ending with $\lambda_{\mathcal{J}} = \lambda_{\min}$. For each λ_j value the inner iteration is run $\mathcal{I}$ times.

4 Convergence and Implementation of the BM3D-MRI algorithm

4.1 Convergence of the BM3D-MRI algorithm

In [30], the convergence to a fixed point has been proven for the iterative, decoupled algorithm (5) under certain conditions. We will utilize this convergence analysis to achieve a similar result for a simplified version of our BM3D-MRI algorithm.

We consider the BM3D-MRI algorithm, with the assumption that the analysis frame and the regularization parameter are kept constant, that is $\mathbf{\Phi}_i = \mathbf{\Phi}$ and

Algorithm 1 BM3D-MRI Algorithm

Input: Observation, $\mathbf{y} = \boldsymbol{\mathcal{F}}_u \mathbf{x}^\star + \boldsymbol{\eta}$; α, $\lambda_{\max}$, $\lambda_{\min}$.

1: Initialize: $\mathbf{x}^0 = \boldsymbol{\mathcal{F}}_u^H \mathbf{y}$.
2: Initialize: $\lambda_1 = \lambda_{\max}$, $\varDelta = \exp\left(\frac{\ln(\lambda_{\max}) - \ln(\lambda_{\min})}{\mathcal{J}-1}\right)$.
3: **for** $j := 1, 2, \dots \mathcal{J}$ **do** ▷ parameter iteration
4: $\mathbf{x}_0 = \mathbf{x}^{j-1}$. ▷ warm start initialization
5: $\lambda_{j+1} = \lambda_j / \varDelta$. ▷ parameter update
6: **for** $i := 1, 2, \dots \mathcal{I}$ **do** ▷ main iteration
7: $\hat{\mathbf{x}}_i = \underset{\mathbf{x}}{\operatorname{argmin}} \; \|\boldsymbol{\mathcal{F}}_u \mathbf{x} - \mathbf{y}\|_2^2 + \alpha \|\mathbf{x} - \mathbf{x}_{i-1}\|_2^2$
observation fidelity update, solved by:
$$\boldsymbol{\mathcal{F}} \hat{\mathbf{x}}_i = \begin{cases} \boldsymbol{\mathcal{F}} \mathbf{x}_{i-1} & \text{, if } k \notin \boldsymbol{\Omega} \\ \dfrac{\boldsymbol{\mathcal{F}} \boldsymbol{\mathcal{F}}_u^H \mathbf{y} + \alpha \boldsymbol{\mathcal{F}} \mathbf{x}_{i-1}}{1+\alpha} & \text{, if } k \in \boldsymbol{\Omega} \end{cases}$$
8: Generate $\boldsymbol{\Phi}_i$ and $\boldsymbol{\Psi}_i$ using $\hat{\mathbf{x}}_i$. ▷ frame update
9: $\mathbf{x}_i = \underset{\mathbf{x}}{\operatorname{argmin}} \; \|\mathbf{x} - \hat{\mathbf{x}}_i\|_2^2 + \lambda_j \|\boldsymbol{\Phi}_i \mathbf{x}\|_0$
model fidelity update: $\mathbf{x}_i \approx \boldsymbol{\Psi}_i \lfloor \boldsymbol{\Phi}_i \hat{\mathbf{x}}_i \rfloor_{\lambda_j}$
10: **end for** ▷ end of inner iteration
11: $\mathbf{x}^j = \mathbf{x}_{\mathcal{I}}$. ▷ image update
12: **end for** ▷ end of main iteration
13: Output reconstructed MR image $\mathbf{x} = \mathbf{x}_{\mathcal{J}}$.

$\lambda_j = \lambda$. Now, the observation and model fidelity steps of the simplified BM3D-MRI algorithm can be written in the following form:

$$\mathbf{S}_o(\boldsymbol{f}) = \underset{\mathbf{x}}{\operatorname{argmin}} \; \|\boldsymbol{\mathcal{F}}_u \mathbf{x} - \mathbf{y}\|_2^2 + \alpha \|\mathbf{x} - \boldsymbol{f}\|_2^2. \tag{15a}$$

$$\mathbf{S}_m(\boldsymbol{f}) = \underset{\mathbf{x}}{\operatorname{argmin}} \; \|\mathbf{x} - \boldsymbol{f}\|_2^2 + \lambda \|\boldsymbol{\Phi} \mathbf{x}\|_p \;. \tag{15b}$$

Using these operators, the simplified BM3D-MRI iteration can be succinctly summarized.

$$\mathbf{x}_i = \mathbf{S}_m\big(\mathbf{S}_o(\mathbf{x}_{i-1})\big) = \mathbf{S}(\mathbf{x}_{i-1}) \tag{16}$$

In [30] it is shown that for a full-rank observation matrix, such as $\boldsymbol{\mathcal{F}}_u$, the $\mathbf{S}_o$ operator is firmly non-expansive for $\alpha > 0$. It is also proven that for a positive regularization parameter λ, if the function $\rho(\mathbf{x}) = \|\boldsymbol{\Phi}\mathbf{x}\|_p$ is convex and semi-continuous, then the operator $\mathbf{S}_m$ will also be firmly non-expansive (Lemma 3.3, [30]). Hence, the $\mathbf{S}_m$ operator (15b) will be firmly non-expansive for $p \geq 1$. When both operators $\mathbf{S}_o$ and $\mathbf{S}_m$ are firmly non-expansive, the composite operator $\mathbf{S} = \mathbf{S}_m \mathbf{S}_o$ will be β-averaged non-expansive for some $\beta \in (0, 1)$ (Lemma 3.2, [30]). Theorem 2.1 in [2] (reiterated as Theorem 3.5 in [30]) states that a β-averaged non-expansive operator (such as $\mathbf{S}$ in (16)) will converge to a fixed point, assuming there is one. Hence, we can state the final convergence result for the simplified BM3D-MRI iteration of (16) as follows.

Theorem 1 *Let $\lambda > 0$, $\alpha > 0$ and $p \geq 1$. Assume that the set of the fixed points of $\mathbf{S}$ is nonempty. Then, the iteration in (16) will converge to a fixed point.*

Theorem 1 suggests that under certain assumptions the BM3D-MRI algorithm converges to a fixed point.

4.2 Implementation aspects for the BM3D-MRI algorithm

The model fidelity steps 8-9 of Alg. 1 simply correspond to BM3D shrinkage based denoising of the image $\hat{\mathbf{x}}_i$. We opted to realize this model fidelity update using the highly optimized BM3D denoising code made available online[1] by the authors of [7]. Again, we only used the 3D transform shrinkage part of BM3D denoising which realizes (13), avoiding further Wiener collaborative filtering.

In our simulations we utilized the default parameter and transform selection as advised by the available BM3D denosing code. Hence, we used a separable 3D transform, with a 2D intrablock transform defined over the blocks, and a 1D interblock transform defined over the third dimension of the patch groups. The 2D transform is chosen as a bi-orthogonal spline wavelet transform, where the decomposing and reconstructing wavelet functions have vanishing moments of order 1 and 5, respectively. The 1D transform over the third group dimension is the Haar transform. The algorithm is implemented with $p = 0$, hence the coefficient shrinkage (14) is realized by hard thresholding with the parameter λ_j.

The regularization parameter λ_j which determines the amount of shrinkage is reduced as iterations proceed. This varying regularization allows for adaptive learning of the image model as the algorithm progresses. A similar approach has been adopted in the deterministic annealing inspired image restoration algorithm of [18] and [19]. In [19], it is suggested that a gradual change in the regularization or "temperature" parameter enables the algorithm to discover different structures in the restored image. A similar approach of changing the regularization parameter was also adopted in [13], where an expectation maximization (EM) algorithm for image inpainting and superresolution was developed. In our simulations, we have found out that diminishing the regularization parameter gives better results when compared to a constant or increasing parameter sequence. In our algorithm, the regularization parameter λ_j determines the severity of thresholding in the model fidelity step. We can state that with decreasing λ_j, the

[1] http://www.cs.tut.fi/foi/GCF-BM3D

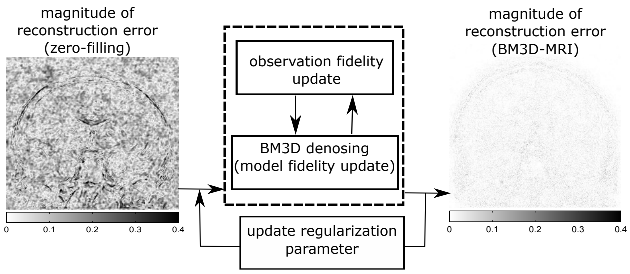

Fig. 1 Graphical outline of the BM3D-MRI algorithm.

algorithm identifies the transform domain coefficients in the groupwise spectrum $\boldsymbol{\omega}$ starting from the most significant ones. The algorithm steadily adds in the less significant coefficients as the regularization slackens. In our simulations, we decreased the λ_j parameter uniformly on a logarithmic scale starting from an initial maximum value and ending with a minimum value at the final iteration. We determined that this logarithmic decrease gave better results when compared with a linear change in the same parameter interval. For the inner iteration we used varying number of iterations $\mathcal{I}_j$, starting from 1 and ending with 10. A basic graphical outline of the BM3D-MRI algorithm is given in Fig 1.

4.3 Complexity of the BM3D-MRI algorithm

The observation fidelity update as realized by (12) dictates the application of forward and inverse Fourier transforms. Hence, it necessitates $\mathcal{O}\big(N\log(N)\big)$ operations. The frame operators in the model fidelity update (13) are highly overcomplete with $M \gg N$. However, due to the structured nature of these frames, the complexity of this step comes out to be linear in the number of pixels of the image, that is $\mathcal{O}(N)$ [11]. In our simulations we have observed that the execution time for a BM3D-MRI iteration is dominated by the model fidelity update realized through BM3D denoising.

4.4 Comparison with existing algorithms

There are nonlocal, patch similarity based MRI reconstruction algorithms proposed in the literature. LOST algorithm of [1] and the more recent PANO algorithm of [25] are two examples for these nonlocal approaches. The LOST algorithm employs a sequence of shrinkage iterations based on hard thresholding followed by subsequent Wiener filtering iterations. In PANO algorithm variable splitting approach is utilized together with linear conjugate gradient iterations. Another similar reconstruction algorithm is the Compressed Sensing Image Reconstruction via Recursive Spatially Adaptive Filtering (CS-RSAF) [12]. CS-RSAF is a recursive algorithm, where for each iteration a denoising filter is applied after the injection of random noise. The denoising filter realizes a nonparametric image model [12].

Both of the LOST [1] and PANO [25] algorithms implicitly utilize the block matching structure of BM3D as the image model. The PANO algorithm in particular provides very competitive MRI reconstruction results, which showcases the power of the nonlocal patch-similarity based image model. Our algorithm is different from all these approaches, as we introduce a distinct decoupling of the overall reconstruction problem. In this decoupled BM3D-MRI algorithm, the BM3D based model fidelity and the observation fidelity steps are clearly separated. The model fidelity step explicitly simplifies to a basic BM3D denoising procedure. Our algorithm allows a simple way to sequentially vary the regularization parameter λ, which enables the algorithm to converge to better reconstructions. The decoupling methodology in BM3D-MRI also allows a simple convergence analysis.

5 Simulation Results

In the simulations four images from the literature are used. Two of the images are a brain MR image and a bust MR image which have been adopted from [17]. Another image is a T2-weighted brain image which has also been utilized in [25], where the details for the acquisition process are given. The fourth and final image is a synthetic phantom image. All images are fixed to be real and positive valued, and they are normalized as to have a maximum pixel value of unity. The sampling in the Fourier domain is realized using three different downsampling strategies, namely random, radial and Cartesian sampling. The downsampling ratio κ/N is varied over two values, 20% and 30%. Fig. 2 shows the example random and radial undersampling masks in the k-space and also the four original images. No observation noise is considered in this setting.

We compare the MRI reconstruction performance of the proposed BM3D-MRI algorithm with recent, sparsity based algorithms from the literature. The compared methods include the shift-invariant discrete wavelet transform based MR reconstruction (SIDWT) method and the nonlocal patch similarity based PANO method from [25][2]. Another method we realized for comparison is the Fast Composite Splitting Algorithm (FCSA) [17][3]. FCSA considers the cost function (4) which enforces both wavelet domain and TV seminorm sparsity. FCSA

[2] http://www.quxiaobo.org/index_publications.html
[3] http://ranger.uta.edu/~huang/R_CSMRI.htm

Table 1 Reconstruction SNR in dB for different sampling masks under 20% random sampling.

Image	Brain			Bust			T2-weighted Brain			Phantom		
Mask	Random	Radial	Cart.	Random	Radial	Cart.	Random	Radial	Cart.	Random	Radial	Cart.
Zero-filled	8.67	10.55	9.41	8.00	8.65	7.69	7.98	9.91	9.73	13.42	18.80	18.51
SIDWT	14.86	14.96	10.32	18.07	16.54	9.56	19.73	18.29	11.68	21.56	26.02	20.32
FCSA	21.87	17.49	10.93	22.02	18.08	10.64	19.57	17.90	12.02	23.72	22.62	19.92
PANO	22.43	18.93	11.95	22.75	20.26	11.95	22.17	21.11	14.16	29.18	29.21	22.03
CS-RSAF	23.32	20.77	**12.46**	21.93	21.21	**13.45**	21.37	21.99	**16.67**	28.72	**29.61**	**26.49**
BM3D-MRI	**25.55**	**21.42**	12.25	**24.47**	**22.44**	12.67	**23.64**	**23.70**	15.21	**29.74**	29.18	24.34

Table 2 Reconstruction SNR in dB for different sampling masks under 30% random sampling.

Image	Brain			Bust			T2-weighted Brain			Phantom		
Mask	Random	Radial	Cart.	Random	Radial	Cart.	Random	Radial	Cart.	Random	Radial	Cart.
Zero-filled	13.34	12.69	11.40	12.60	10.19	9.77	12.64	11.55	11.86	20.38	19.68	20.31
SIDWT	21.64	19.17	13.25	23.42	20.73	13.27	23.82	22.91	16.40	29.85	28.88	23.69
FCSA	26.95	22.77	14.03	25.81	22.71	13.74	23.35	22.73	15.83	27.65	25.41	22.33
PANO	27.02	23.94	15.63	26.60	24.29	15.85	26.26	25.54	19.60	**31.20**	**30.94**	23.97
CS-RSAF	27.06	25.28	**16.97**	25.68	24.60	**18.04**	24.83	25.40	21.91	30.86	30.71	**30.34**
BM3D-MRI	**29.38**	**26.77**	16.64	**28.28**	**26.72**	17.43	**28.09**	**28.32**	**22.47**	30.87	30.40	28.08

uses a composite algorithm with both operator and variable splitting. We have also implemented the CS-RSAF reconstruction algorithm from [12]. In [12], only the simulation setup with radial samples in the Fourier domain was considered, which simulates Radon projections. Here, we have adapted the publicly available code[4] for CS-RSAF algorithm to our simulation setting. We also list the results for the zero-filling based reconstruction as a benchmark. SNR (signal-to-noise ratio) is the main measure for performance, and SNR in dB is calculated as follows.

$$\mathrm{SNR} = 10\log_{10}\frac{\|\mathbf{x}\|_2^2}{\|\mathbf{x}^\star - \mathbf{x}\|_2^2} \tag{17}$$

The number of outer iterations has been set as $\mathcal{J} = 40$ for FCSA and $\mathcal{J} = 20$ for BM3D-MRI. FCSA employs regularization parameters $\beta_1 = 10^{-4}$ and $\beta_2 = 10^{-4}$ for (4). All the other parameters for SIDWT, PANO and FCSA algorithms are set using the default values from their publicly available codes. PANO has been realized using the setting where the guide image is reconstructed from the available data. For CS-RSAF the parameters for exponential decay of excitation noise are set as $\alpha = (1+1/300)^2$ and $\beta = 1000$. The total number of iterations for CS-RSAF is chosen as 500. For BM3D-MRI the initial and final regularization parameters are chosen as $\lambda_{\max} = 200/255$ and $\lambda_{\min} = 1/255$, respectively. The observation fidelity parameter for BM3D-MRI is $\alpha = 0$. All these parameters are kept constant over the whole range of different simulation settings. Hence, we did not optimize the parameters for particular simulation settings. The simulations were executed in Matlab on a computer with an Intel i7 CPU at 1.8GHz, 8GB memory and 64-bit operating system.

[4] http://www.cs.tut.fi/~comsens/

Table 3 Time required for the algorithms.

Algorithm	BM3D-MRI	FCSA	SIDWT	PANO	CS-RSAF
Time (sec)	13.9	0.74	50.8	98.9	167.4

Table 1 details the SNR performance of the four algorithms for three different mask types with 20% downsampling. Table 2 details the corresponding results for 30% downsampling. The results for the zero-filling based reconstruction are also listed. In both Tables 1 and 2, the best SNR result in each column is denoted with bold case. For both downsampling ratios the BM3D-MRI outperforms the other four algorithms for most image and mask type combinations. Table 3 presents the overall time required by each algorithm for the sample case of brain image and 20% random downsampling. Our implementation of BM3D-MRI is about one order slower than the highly optimized realization of FCSA. However, BM3D-MRI is faster than the SIDWT, CS-RSAF and PANO algorithms. Hence, BM3D-MRI presents a good trade-off between runtime complexity and performance.

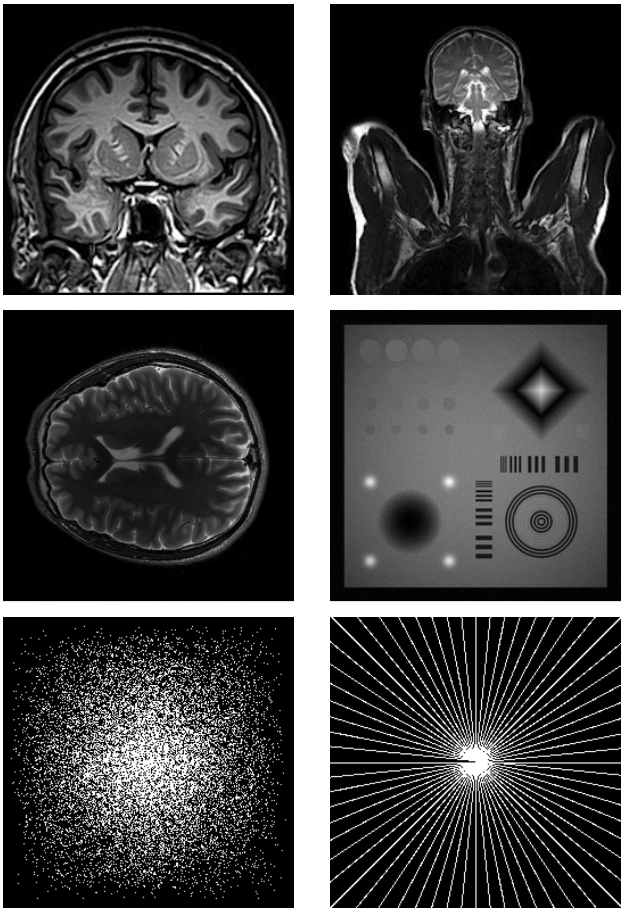

Fig. 2 Original test images and sampling mask examples. First row: Brain and bust images [17]. Second row: T2-weighted brain [25] and phantom images. Third row: Random and radial sampling masks.

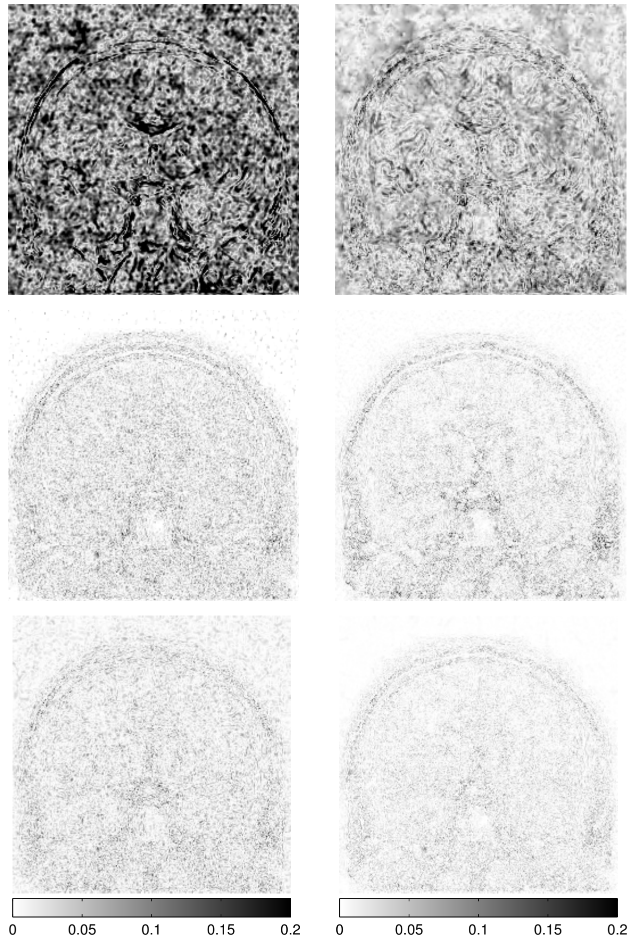

Fig. 3 Magnitude of reconstruction error for brain image under 20% random sampling. In each of the following images: first row, zero-filling (left), SIDWT [25] (right); second row, FCSA [17] (left), CS-RSAF [12] (right); third row, PANO (left) [25], BM3D-MRI (right).

Figs. 3 through 6 present the error or difference images $|\mathbf{x} - \mathbf{x}^{\star}|$ for the simulations, for which reconstruction SNR has been given in Table 1. In all of these figures, first row includes the SIDWT (left) and FCSA (right) results, whereas second row includes the PANO (left) and BM3D-MRI (right) results. The error images are visualized using an inverted colormap, where higher error intensities correspond to darker pixels. The error images corroborate the SNR results, and the error images for BM3D-MRI have in general a lighter coloring indicating less energy in the error signal when compared to the other algorithms. Fig. 7 presents the dependence of the reconstruction error on the α value when all the other variables are fixed constant. Fig. 8 on the other hand depicts the change of the reconstruction error with the $\lambda_{\max}$ parameter. The results are for 20% random sampling. BM3D-MRI performance degrades when these parameters are chosen non-optimally. For different α values, choosing specific values for the iteration numbers helps to improve final SNR performance. However, we have observed that the best reachable SNR result still consistently deteriorates as we get further from the optimal α value (in this case $\alpha = 0$).

The SNR results and the presented error images indicate that the BM3D-MRI algorithm has superior reconstruction performance when compared to the considered powerful compressed sensing based algorithms. The nonlocal, adaptive BM3D image model successfully competes with the popular, wavelet and TV based static image model from the literature. BM3D-MRI has similar or better performance and is faster when compared to the recent, state-of-the-art PANO and CS-RSAF algorithms, which also utilize nonlocal similarities in the reconstructed image.

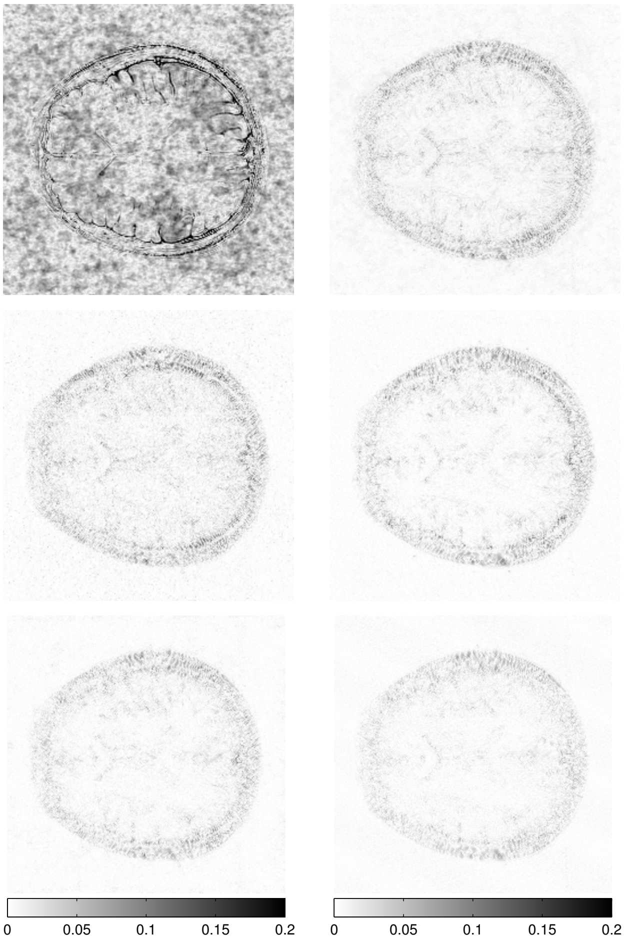

Fig. 4 Magnitude of reconstruction error for T2 weighted brain image [25] under 20% random sampling.

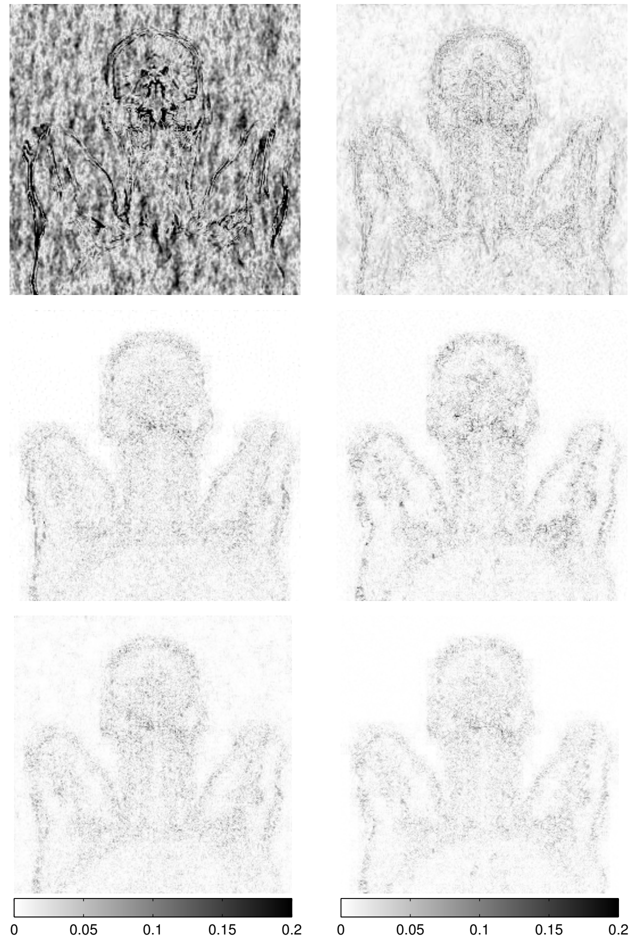

Fig. 5 Magnitude of reconstruction error for bust image under 20% random sampling.

6 Conclusions

We have presented a novel algorithm for MRI reconstruction by using the nonlocal BM3D image model. The developed BM3D-MRI algorithm comprises fully decoupled observation fidelity and model fidelity steps. This decoupling permits the adoption of a varying regularization parameter strategy, which enhances the performance. The finalized algorithm is relatively lucid and easy to apprehend with only three parameters which do not require fine tuning. The convergence of BM3D-MRI to a fixed point is also proven under certain assumptions. The MRI reconstruction performance of BM3D-MRI is compared with recent sparsity based algorithms from the literature. BM3D-MRI consistently outperforms the competing algorithms under different sampling masks and sampling ratios for a variety of images. Hence, the nonlocal BM3D image model is shown to be a valuable addition to the arsenal of possible image priors and regularization methods for MRI reconstruction from heavily undersampled observations. The method proposed here might be readily extended to other inverse reconstruction problems in imaging by changing the observation fidelity step depending on the acquisition process of the imaging problem under consideration.

References

1. Akçakaya, M., Basha, T.A., Goddu, B., Goepfert, L.A., Kissinger, K.V., Tarokh, V., Manning, W.J., Nezafat, R.: Low-dimensional-structure self-learning and thresholding: Regularization beyond compressed sensing for MRI reconstruction. Magnetic Resonance in Medicine **66**(3), 756–767 (2011)
2. Byrne, C.: A unified treatment of some iterative algorithms in signal processing and image reconstruction. Inverse Problems **20**(1), 103–120 (2004)
3. Chambolle, A., De Vore, R., Lee, N.Y., Lucier, B.: Nonlinear wavelet image processing: variational problems, compression, and noise removal through wavelet shrinkage. IEEE Trans. Image Process. **7**(3), 319–335 (1998). DOI 10.1109/83.661182
4. Chambolle, A., Lions, P.L.: Image recovery via total variation minimization and related problems. Nu-

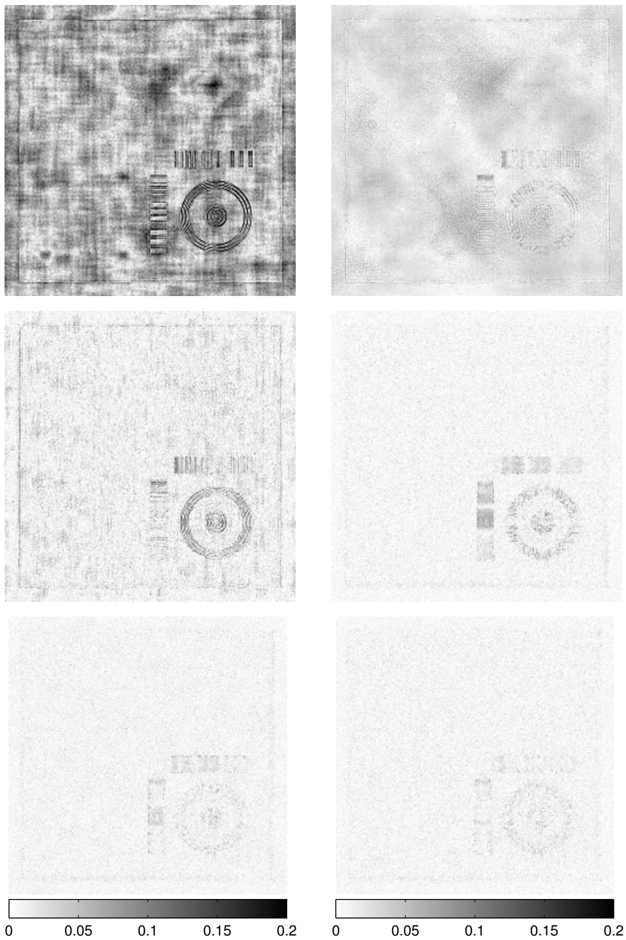

Fig. 6 Magnitude of reconstruction error for phantom image under 20% random sampling.

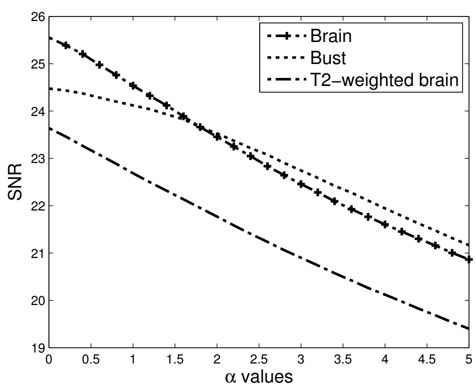

Fig. 7 Reconstruction SNR in dB for BM3D-MRI with varying α values in the case of 20% random sampling.

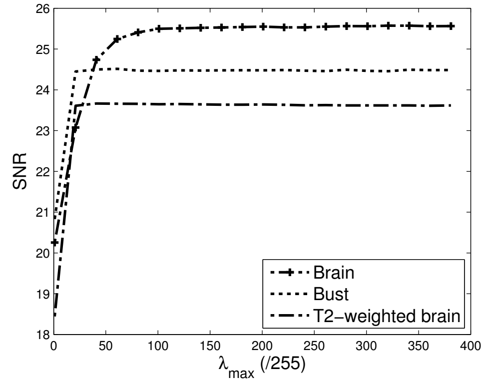

Fig. 8 Reconstruction SNR in dB for BM3D-MRI with varying $\lambda_{\max}$ values in the case of 20% random sampling.

merische Mathematik **76**(2), 167–188 (1997). DOI 10.1007/s002110050258. URL http://dx.doi.org/10.1007/s002110050258

5. Combettes, P., Pesquet, J.: A Douglas-Rachford splitting approach to nonsmooth convex variational signal recovery. IEEE J. Sel. Topics Signal Process. **1**(4), 564–574 (2007). DOI 10.1109/JSTSP.2007.910264
6. Crandall, R., Bilgin, A.: Lossless image compression using causal block matching and 3d collaborative filtering. In: Image Processing (ICIP), 2014 IEEE International Conference on, pp. 5636–5640 (2014). DOI 10.1109/ICIP.2014.7026140
7. Dabov, K., Foi, A., Katkovnik, V., Egiazarian, K.: Image denoising by sparse 3-d transform-domain collaborative filtering. IEEE Trans. Image Process. **16**(8), 2080–2095 (2007). DOI 10.1109/TIP.2007.901238
8. Dabov, K., Foi, A., Katkovnik, V., Egiazarian, K.: Image restoration by sparse 3d transform-domain collaborative filtering. In: Proc. SPIE, vol. 6812, pp. 1–12 (2008)
9. Danielyan, A., Foi, A., Katkovnik, V., Egiazarian, K.: Image upsampling via spatially adaptive block-matching filtering. In: Signal Processing Conference, 2008 16th European, pp. 1–5 (2008)
10. Danielyan, A., Katkovnik, V., Egiazarian, K.: Image deblurring by augmented Lagrangian with BM3D frame prior. Workshop on Information Theoretic Methods in Science and Engineering (WITMSE), Tampere, Finland pp. 16–18 (2010)
11. Danielyan, A., Katkovnik, V., Egiazarian, K.: BM3D frames and variational image deblurring. IEEE Trans. Image Process. **21**(4), 1715–1728 (2012). DOI 10.1109/TIP.2011.2176954
12. Egiazarian, K., Foi, A., Katkovnik, V.: Compressed sensing image reconstruction via recursive spatially adaptive filtering. In: Image Processing (ICIP), 2007 IEEE International Conference on, vol. 1, pp. 549–552 (2007)
13. Fadili, M.J., Starck, J.L., Murtagh, F.: Inpainting and zooming using sparse representations. The Computer Journal **52**(1), 64–79 (2007)
14. Goldstein, T., Osher, S.: The split Bregman method for L1-regularized problems. SIAM Journal on Imaging Sciences **2**(2), 323–343 (2009)
15. Griswold, M.A., Jakob, P.M., Heidemann, R.M., Nittka, M., Jellus, V., Wang, J., Kiefer, B., Haase, A.: Generalized autocalibrating partially parallel acquisitions (grappa). Magnetic Resonance in Medicine **47**(6), 1202–1210 (2002). DOI 10.1002/mrm.10171
16. Gunturk, B.K., Li, X. (eds.): Image Restoration: Fundamentals and Advances. CRC Press (2012)
17. J.Huang, S.Zhang, D.Metaxas: Efficient MR image reconstruction for compressed MR imaging. Medical Image Analysis **15**(5), 670–679 (2011). DOI http://dx.doi.org/10.1016/j.media.2011.06.001
18. Li, X.: Fine-granularity and spatially-adaptive regularization for projection-based image deblurring. IEEE

Trans. Image Process. **20**(4), 971–983 (2011). DOI 10.1109/TIP.2010.2081681
19. Li, X.: Image recovery via hybrid sparse representations: A deterministic annealing approach. IEEE J. Sel. Topics Signal Process. **5**(5), 953–962 (2011). DOI 10.1109/JSTSP.2011.2138676
20. Lustig, M., Donoho, D., Pauly, J.: Sparse MRI: The application of compressed sensing for rapid MR imaging. Magnetic Resonance in Medicine **58**(6), 1182–1195 (2007)
21. Lustig, M., Donoho, D., Santos, J., Pauly, J.: Compressed sensing MRI. Signal Processing Magazine, IEEE **25**(2), 72–82 (2008). DOI 10.1109/MSP.2007.914728
22. Ma, S., Yin, W., Zhang, Y., Chakraborty, A.: An efficient algorithm for compressed MR imaging using total variation and wavelets. In: Computer Vision and Pattern Recognition, 2008. CVPR 2008. IEEE Conference on, pp. 1–8 (2008). DOI 10.1109/CVPR.2008.4587391
23. Pruessmann, K.P., Weiger, M., Scheidegger, M.B., Boesiger, P.: Sense: Sensitivity encoding for fast mri. Magnetic Resonance in Medicine **42**(5), 952–962 (1999)
24. Qu, X., Cao, X., Guo, D., Hu, C., Chen, Z.: Combined sparsifying transforms for compressed sensing MRI. Electronics Letters **46**(2), 121–123 (2010). DOI 10.1049/el.2010.1845
25. Qu, X., Hou, Y., Lam, F., Guo, D., Zhong, J., Chen, Z.: Magnetic resonance image reconstruction from undersampled measurements using a patch-based nonlocal operator. Medical Image Analysis **18**(6), 843–856 (2014)
26. Ravishankar, S., Bresler, Y.: MR image reconstruction from highly undersampled k-space data by dictionary learning. IEEE Trans. Med. Imag. **30**, 1028–1041 (2011)
27. Setzer, S.: Operator splittings, Bregman methods and frame shrinkage in image processing. Int. J. Comput. Vision **92**(3), 265–280 (2011)
28. Sreehari, S., Venkatakrishnan, S.V., Drummy, L.F., Simmons, J.P., Bouman, C.A.: Advanced prior modeling for 3d bright field electron tomography. Proc. SPIE **9401**, 940,108–1–940,108–12 (2015)
29. Tan, J., Ma, Y., Baron, D.: Compressive imaging via approximate message passing with image denoising. IEEE Trans. Signal Process. **63**(8), 2085–2092 (2015)
30. Wen, Y.W., Ng, M.K., Ching, W.K.: Iterative algorithms based on decoupling of deblurring and denoising for image restoration. SIAM Journal on Scientific Computing **30**(5), 2655–2674 (2008)
31. Yang, J., Zhang, Y., Yin, W.: A fast alternating direction method for TVL1-L2 signal reconstruction from partial Fourier data. IEEE J. Sel. Topics Signal Process. **4**(2), 288–297 (2010). DOI 10.1109/JSTSP.2010.2042333